Aerosol Science and Technology

ISSN: 0278-6826 (Print) 1521-7388 (Online) Journal homepage: www.tandfonline.com/journals/uast20

Derivation of models for the fusing of soot aggregates from carbon black reactor data

Daniel O'Sullivan, Russell B. Diemer Jr. & Stelios Rigopoulos

To cite this article: Daniel O'Sullivan, Russell B. Diemer Jr. & Stelios Rigopoulos (2025) Derivation of models for the fusing of soot aggregates from carbon black reactor data, Aerosol Science and Technology, 59:4, 451-469, DOI: 10.1080/02786826.2025.2450209

To link to this article: https://doi.org/10.1080/02786826.2025.2450209

AEROSOL SCIENCE AND TECHNOLOGY
2025, VOL. 59, NO. 4, 451–469
https://doi.org/10.1080/02786826.2025.2450209

Derivation of models for the fusing of soot aggregates from carbon black reactor data

Daniel O'Sullivan[a], Russell B. Diemer Jr.[b], and Stelios Rigopoulos[a]

[a]Department of Mechanical Engineering, Imperial College London, London, UK; [b]Department of Chemical and Biomolecular Engineering, University of Delaware, Newark, Delaware, USA

ABSTRACT

Soot aggregate fusing models have rarely been employed in sooting flame simulations. Previously, such models have been based on sintering models of inorganic nanoparticles (silica/titania). The objective of the present article is to derive a soot fusing model from a graphitic material, namely carbon black. While there are differences between soot and carbon black, the significant similarities allow a carefully selected group of carbon black grades to function as a soot-proxy for the derivation of a fusing model. Two appropriate subsets of carbon black grades are found, with the key difference being the relative amounts of surface oxygen content in each subset. The later stage of the furnace black reactor process is characterized by the direct competition of aggregation and fusing in an oxygen and fuel starved environment. This serves as the basis for an inverse population balance approach, that allows the characteristic fusing timescale to be determined for a given set of input reactor conditions. Two fusing models are produced each corresponding to the subset of carbon black grades and reactor conditions used. A linear relationship between the characteristic fusing timescale and primary particle diameter was found in both models. The models are used to simulate several inert reheating experiments with four different soot samples. Each fusing model can predict well the experimentally observed fusing behavior of soot samples that corresponded closest to the composition of the original carbon black data employed for its derivation.

ARTICLE HISTORY
Received 17 June 2024
Accepted 2 December 2024

EDITOR
Jason Olfert

1. Introduction

Soot emissions arise due to incomplete combustion and play an important role in many atmospheric and climate models due to their light absorbing properties (Bond and Bergstrom 2006) and relatively long atmospheric lifetimes (Wolff 1985; Ogren 1982). Carbonaceous aerosols have been identified as the "*second most important human emission in terms of its climate forcing*" after carbon dioxide (Bond et al. 2013), and IPCC (2014) further identifies soot as the most important particulate component to global warming. Inhaled soot emissions are well documented to cause many adverse health effects from respiratory damage to increased cancer risk (Niranjan and Thakur 2017).

Whereas early approaches assume that soot particles have an overall spherical shape, in reality, soot forms fractal aggregates where spherical primary particles assemble into *aciniform* or chain-like structures. When accounted for, the fractal morphology of soot aggregates produces a significant increase in lung deposition relative to their spherical equivalents and alters the deposition patterns within the respiratory tract (Broday and Rosenzweig 2011). Fractal aggregates have a greater surface area than their spherical equivalents, and surface area is a key input into many lung deposition estimates from road traffic pollution (Vu et al. 2018). Moreover, the large specific surface area of soot aggregates leads to increased reactivity, and hence toxicity when biological systems are exposed to soot (Tang et al. 2024; Li et al. 2023). It is also widely recognized that a large degree of uncertainty surrounds the optical properties of atmospheric soot in global circulation models (Bond et al. 2013; IPCC 2014), and aggregate morphology has been identified as one of the main sources of this uncertainty (Bond and Bergstrom 2006; Adachi, Chung, and Buseck 2010; Forestieri et al. 2018; Liu and Mishchenko 2018). Recent efforts have proved that

CONTACT Stelios Rigopoulos s.rigopoulos@imperial.ac.uk Department of Mechanical Engineering, Imperial College London, Exhibition Road, London, SW7 2AZ, UK.

morphology matters more than previously thought, and studies have focussed on detailing the effect of fractal aggregates and an evolving morphology throughout the lifetime of atmospheric soot (He 2019). Whereas soot aggregates undergo a variety of atmospheric processes, the *near-source* particles are the primary concern of the present work. An understanding of near-source soot morphology serves as a starting point for subsequent models of atmospheric soot.

In laboratory settings, light extinction experimental techniques have been used to measure soot volume fraction but rely on *a priori* knowledge of the refractive index of the aggregates, which in turn is a function of aggregate morphology and soot composition. Soot aggregates have often been considered as spherical in the context of models, to invert light extinction readings into soot volume fraction results, and the discrepancy due to the fractal nature of soot aggregates is explained clearly in Kelesidis and Pratsinis (2022) alongside a novel method to quantify the varying refractive index of soot aggregates in the context of sooting flames.

Soot aggregate morphology is determined by several simultaneous particulate processes in flames; namely aggregation, surface growth and oxidation, and fusing. The evolution of the soot properties, such as particle size and morphology can be described *via* a population balance equation (PBE), which expresses the evolution of the distribution of soot properties as a result of the aforementioned kinetic processes, as well as by transport in physical space; more information, particularly in the context of soot, can be found in Rigopoulos (2019, 2024).

The present work focusses on fusing, which is a process that results in a reduction of the surface area of aggregates. The exact mechanism by which this occurs may vary in the case of soot. In certain cases, if temperatures experienced by aggregates supersede the melting temperature of the material in question, then liquid-like behavior ensues with what could be correctly described as coalescence. When aggregate neck formation is analyzed, sintering is often used to describe solid-like behavior. In the case of soot aggregates, a question is whether soot behaves in a liquid-like or a solid-like manner, which may depend on whether incipient or mature soot is considered. Processes, such as coalescence and sintering can all be described as surface area minimization processes, governed by a linear rate law in terms of aggregate surface area, and a constant of proportionality expressed as the reciprocal of a characteristic time. In the present work, the term "fusing" is used as a generic term to describe processes, without reference to the specific mechanism and material properties of soot, inline with the comments of Michelsen et al. (2020). The characteristic fusing time is itself a function of temperature, primary particle size, and other kinetic parameters. Determining an expression for this timescale for soot is the main focus of this article.

Fusing has received very limited attention so far in the context of soot population balance models. By contrast, it is a major part of models for inorganic nanoparticle synthesis, where often the evolution of aggregate properties is determined by a competition between aggregation and sintering. Its role in soot formation processes is not so clear, due to the presence of a wider range of more kinetic processes (nucleation, condensation, surface growth, and oxidation). At present, there is no established expression for the soot fusing timescale. The majority of sooting flame predictions do not include finite-rate fusing due to limitations in the PBE forms employed. For example, it may be assumed that particles are spherical or that there is an instantaneous change between spherical and fractal aggregates at a certain particle size. To include finite-rate fusing, the model must include account for the evolution of the surface area of aggregates or the number of primary particles explicitly. Only two fusing timescale models have been used to predict the size and morphology of soot aggregates in flames. As discussed below, both of these fusing models originate from work involving materials other than soot (titania and silica). An exception is the recent work of Matsukawa et al. (2023), where a fusing model was obtained from experimental data on ethylene-derived and benzene-derived soot in a pyrolitic reactor. However, the fusing model of Matsukawa et al. (2023) has not been implemented in a sooting flame simulation at the time of writing.

Veshkini, Dworkin, and Thomson (2016) presented an expression for the characteristic fusing timescale of soot based on an expression previously used to simulate titania aggregates (Xiong, Kamal Akhtar, and Pratsinis 1993). This expression has its origins in the experimental work of Kobata, Kusakabe, and Morooka (1991), who determined the fourth order scaling with primary particle diameter as well as the relevant values for the activation temperature and pre-exponential factor while studying titania aggregates. Veshkini, Dworkin, and Thomson (2016) used this expression and the titania-based values for activation energy and pre-exponential factor to simulate the nonsmoking

co-flow diffusion flame of Santoro, Semerjian, and Dobbins (1983).

Chen et al. (2013) proposed a fusing expression based on the works of Shekar et al. (2012) and Tsantilis, Pratsinis, and Briesen (2001) on silica nanoparticles. This expression includes three parameters which were then calibrated against the experimental results of Zhao et al. (2005) in the context of soot, and used to simulate several premixed laminar flames. It also incorporates a cutoff primary particle diameter below which small particles are assumed to fuse instantaneously.

The main concern with the two aforementioned approaches is the suitability of the original fusing expressions to soot, even if the activation energy and relevant fusing parameters have been calibrated in some way. There are a large number for possible mechanisms that could be responsible for soot fusing, either alone or in combination. In the present article, it is thus proposed to employ data originating in a carbonaceous material, such as carbon black, to derive a soot fusing timescale. Carbon black is formed *via* the pyrolysis or incomplete combustion of a hydrocarbon feedstock and is said to be aciniform with aggregates composed of spherical primary particles. Often heavy oils are used, although some specific carbon blacks require more specific feeds, such as acetylene. Various reactor designs and processes exist, but the three main groups are furnace black, thermal black, and acetylene black. The overwhelming majority of carbon black produced is used as reinforcement filler in car tyres, with specialist carbon blacks used in inks, dyes, and conductive filler for electrical applications. When used in car tyres, carbon black aggregates bind to the rubber, and the performance of the particles is determined by their size, morphology, and surface chemistry (Heinrich, Klüppel, and Vilgis 2002; Spahr and Rothon 2015). As a consequence, manufacturers pay close attention to the primary particle diameter and morphology, i.e., the *structure* of the carbon black aggregates produced, alongside the processes which determine it. Grades are assigned to denote the size of primary particles and a manufacturer-specific "level of structure" to indicate the overall morphology of the product (Tunnicliffe 2015).

The objective of the present article is to derive a fusing model for soot from data of an appropriate carbon black proxy. While there is a wide variety of carbon black grades available, it is hypothesized here that, with careful consideration of composition and aggregate structure, a subset of these grades could be used as a proxy for deriving a fusing model for flame generated soot. Accordingly, the first step in the derivation of the model is the choice of suitable carbon black grades for use as proxies. Once the choice of grades has been established, a set of associated reactor conditions, such as residence time, temperature, and primary particle size of the final product is obtained and collated. Subsequently, the new model is derived by employing an inverse population balance approach (Diemer 2023). This method allows us to first determine the most appropriate general form of the mathematical expression and subsequently obtain the values of the parameters. The model (in fact a set of two models) will then be tested by simulating the inert reheating experiment of Ono et al. (2017), where soot aggregates generated from various fuels experience a reduction in mobility diameter due to fusing alone, and compared with the trends in activation energy inferred in the recent work of Matsukawa et al. (2023).

The article commences with an exposition of the general modeling framework for fusing processes and a summary of the models that can be found at present for soot. This is followed by a discussion contrasting the variety of carbon black grades with some representative examples of soot, culminating in the selection of relevant carbon black reactor data that will be employed. The derivation of the new fusing models is shown next. The article concludes with the application of the model to the simulation of the Ono et al. (2017) experiment.

2. Modeling framework for fusing processes and previous models

Fusing, sintering, and coalescence share historical links that often confuse present-day discussions. The coalescence of liquid droplets is driven by the kinetic energy of the colliding droplets being dissipated *via* various mechanisms, such as capillary and viscous forces in an oscillatory manner. The earliest consideration of this oscillatory behavior dates back to the inviscid natural frequency found by Rayleigh (1879). Lamb (1932) extended this approach to include the effects of internal viscous forces which act to damp the oscillation, and in the limit of high viscosity Chandrasekhar (1961) showed that the characteristic timescale for coalescence was proportional to the product of the viscosity and droplet size, while being inversely proportional to surface tension.

The seminal work of Frenkel (1945) proposed describing the sintering of solid particles as the "*the viscous flow of crystalline bodies*." Frenkel's approach

was to consider defects in the crystal lattice and an associated mass diffusion process between two contacting spherical particles, mimicking a viscous flow as previously seen in liquid systems. An associated "*self-diffusion*" coefficient was derived and the entire process was driven by the reduction of free energy.

Subsequent works focussed on the kinetics of neck formation between the two spheres, and are classically known as initial stage sintering or fusing models. German and Munir (1976) were able to describe the overall surface area from an understanding of neck geometry and addressed various sintering mechanisms, such as surface diffusion or lattice diffusion. Hiram and Nir (1983) determined that the final neck size was reached exponentially in time, and thus a linear rate law valid beyond the initial stages of neck growth was proposed. An equivalent linear rate law describing surface area can be deduced by assuming the remaining bulk of the particles, remain spherical throughout the sintering process. Koch and Friedlander (1990) explained how this asymptotic linear rate law describing the evolution of surface area can be used as a good approximation for sintering or fusing at any stage, assuming an underlying viscous flow sintering mechanism. Friedlander and Wu (1994) further re-derived this relationship by rigorously assuming a general solid state diffusion mechanism and solving for the decrease in chemical potential along the surface of two contacting spheres.

The general form of a fusing model is given by an expression where the difference between the surface area of an aggregate, $a(v)$, and that of its spherical equivalent, $a_s(v)$, is proportional to the rate of change of aggregate surface area, Friedlander and Wu (1994), as shown below:

$$\frac{da(v)}{dt} = -\frac{1}{\tau_\sigma}\left(a(v) - a_s(v)\right) \tag{1}$$

where τ_σ is the characteristic fusing timescale and v denotes the volume of an aggregate. Equation (1) can be recast in terms of number of primary particles, as shown below (Rogak 1997):

$$\frac{dn_p(v)}{dt} = -\frac{3}{\tau_\sigma}\left(n_p(v) - n_p^{\frac{2}{3}}(v)\right) \tag{2}$$

Depending on the formulation of the overall population balance used to predict the evolution of the soot particle size distribution, either of these expressions may be employed.

While Equations (1) and (2) describe the general features of a fusing process, the details of the particular mechanism are encapsulated in the fusing timescale, which must be given by another expression. The following equation is a model for a liquid-like coalescence mechanism (Frenkel 1945):

$$\tau_\sigma = \frac{\mu(T)\, d_p}{\sigma} \tag{3}$$

where $\mu(T)$ is the viscosity of the fusing particles, d_p is the particle diameter, and σ is the surface tension. By contrast, the analogous expression for solid-like behavior consistent with a general solid-state diffusion process is the following (Friedlander and Wu 1994):

$$\tau_\sigma = \frac{3}{64\pi}\frac{k_B T v_p}{D(T)\sigma v_{mol}} \tag{4}$$

where k_B is the Boltzmann constant, v_p is the volume of the fusing particles, v_{mol} is molecular volume, σ is the surface tension, and $D(T)$ is the solid-state diffusion coefficient of the dominant mass transport mechanism. Importantly, both the viscosity and the solid-state diffusion coefficient of fusing particles can be viewed as thermally activated processes and thus commonly expressed as Arrhenius laws (Wu et al. 1993). Subsequently, it is expected that an exponential scaling relationship between the fusing timescale and temperature exists, regardless of the material nature of the underlying fusing particles.

As discussed in Section 1, no widely agreed expression for the soot fusing timescale expression exists, and expressions originally derived for other materials have been employed in simulations of sooting flames, though their parameters may be adjusted for soot. The following expression was used by Veshkini, Dworkin, and Thomson (2016), based on titania:

$$\tau_t = A_0\ d_p^4\ T \exp\left(\frac{T_a}{T}\right) \tag{5}$$

Notably, this equation expresses a fourth order dependency of the timescale on the primary particle diameter, with a value for activation temperature, T_a, found to be 33,100 K (Kobata, Kusakabe, and Morooka 1991). Chen et al. (2013) employed a silica-based model, given by the following equation:

$$\tau_s = A_0\ d_p \exp\left[\frac{T_a}{T}\left(1 - \frac{d_c}{d_p}\right)\right] \tag{6}$$

This model has been used to model soot aggregates with a wide range of activation temperatures (18,000–100,000 K). Sun, Rigopoulos, and Liu (2021) explored the sensitivity of the two aforementioned fusing models to activation temperature in the context of a laminar diffusion flame.

Finally, a recent work by Matsukawa et al. (2023) derived a model from a soot reheating experiment.

The model is shown below:

$$\tau_\sigma = A_0 \; d_p^4 \; T \exp\left(\frac{E}{RT}\right) \tag{7}$$

The methodology of Seto, Shimada, and Okuyama (1995) involving titania nanoparticles was used by Matsukawa et al. (2023) to calibrate the activation energy, E, and pre-exponential factor, A_0 in the expression above.

In the present work, a set of two new models for the soot fusing timescale will be derived from a range of data from carbon black reactors, selected from the literature to act as proxy for soot. The derivation will be carried out with an inverse population balance approach that will allow us to determine the most appropriate form of the mathematical expression, in addition to the model parameters. The selection of the data and the justification as to why they are chosen as proxies is detailed in the following section.

3. Carbon black as proxy for soot aggregates

3.1. Procedure for selection of proxy

Since the elemental composition of aggregates is intrinsically linked to fusing kinetics, we have compiled data from a large range of soot samples and carbon black grades. The composition of carbonaceous aggregates in terms of bulk C/H/O content by weight was considered. The C/H ratio is a well-documented method (Santamaria et al. 2010) of quantifying the composition of a soot sample, as the C/H ratio increases the sample can be said to be more graphitic,[1] the lower the C/H ratio the less graphitic the sample is. Furthermore, the C/O ratio describes the surface oxygen content of the primary particles. Commonly found as part of aldehyde, ketone, hydroxy, phenolic, carboxylic, and carbonyl groups (Wang et al. 2013; Setyan, Sauvain, and Rossi 2009), the oxygen content is linked to how water dispersible the aggregates are. For example, PRINTEX U is a colour-black used in ink and dyes and readily disperses in water due to its high oxygen content. Soot occupies a wide range of C/H and C/O (wt%) values, with carbon black grades occupying narrower ranges in composition.

Figure 1 presents 17 soot samples across a wide range of fuels, combustor, and engine configurations. Several sources did not provide enough information to calculate both C/H and C/O (wt%) ratios, in which case a line represents a single ratio; vertical lines represent C/H ratios with unknown C/O ratio and horizontal lines characterize C/O ratios with unknown C/H ratio. The compositional ranges are summarized for soot and each group of carbon black grades in Table 1. A few observations can be readily made from this figure. Carbon black grades are generally more graphitic than soot, the exception being the laboratory-made kerosene soot of Daly and Horn (2009) which has the highest C/H (wt%) of any soot sample considered. However, the three groups of abrasion furnace blacks (HAF, SAF, ISAF) and the channel black examples appear to be bounded within a C/O range consistent with soot. The shaded areas correspond to the maximum and minimum values for both C/H and C/O. Clearly, acetylene and thermal blacks are sufficiently different in both C/H and C/O being almost entirely carbon, and thus cannot be viewed as suitable proxies for soot. The classes of semi-reinforcing, general purpose, and fast extruding furnace black partially overlap with the shaded area corresponding to soot, but as a group have a lower oxygen content than the 3 classes of abrasion furnace blacks. Finally, channel black as a group closely resembles soot in terms of composition, and perhaps this is no surprise as the channel black process is the oldest and simplest one. Channel black can be viewed as the least engineered version of carbon black, closely resembling the natural product soot, whereas acetylene black and thermal black were developed much later and have been highly engineered to maximize the graphitic character of the aggregates, in stark contrast to soot. Furnace blacks sit somewhere in between, with abrasion blacks closely resembling soot in terms of C/O, albeit with a higher C/H than would typically be found for most soot samples. PRINTEX U was included in the analysis as it has been used as a soot proxy in some previous studies and the results presented here agree with this point of view (Boger et al. 2015).

Thus, when considering the primary particle size, specific surface area, and bulk composition of a wide range of soot and carbon black examples, the three abrasion furnace blacks and the channel blacks are taken to be the most similar ones to soot. In the following, these grades and their associated reactor data will be employed to study the soot fusing rate.

3.2. Selection of furnace black reactor data

With abrasion furnace blacks and channel blacks set as the soot proxies, reactor data has to be collected that describes the reactor temperature, residence time,

[1]The term "carbonised" can be equivalently used in this sense.

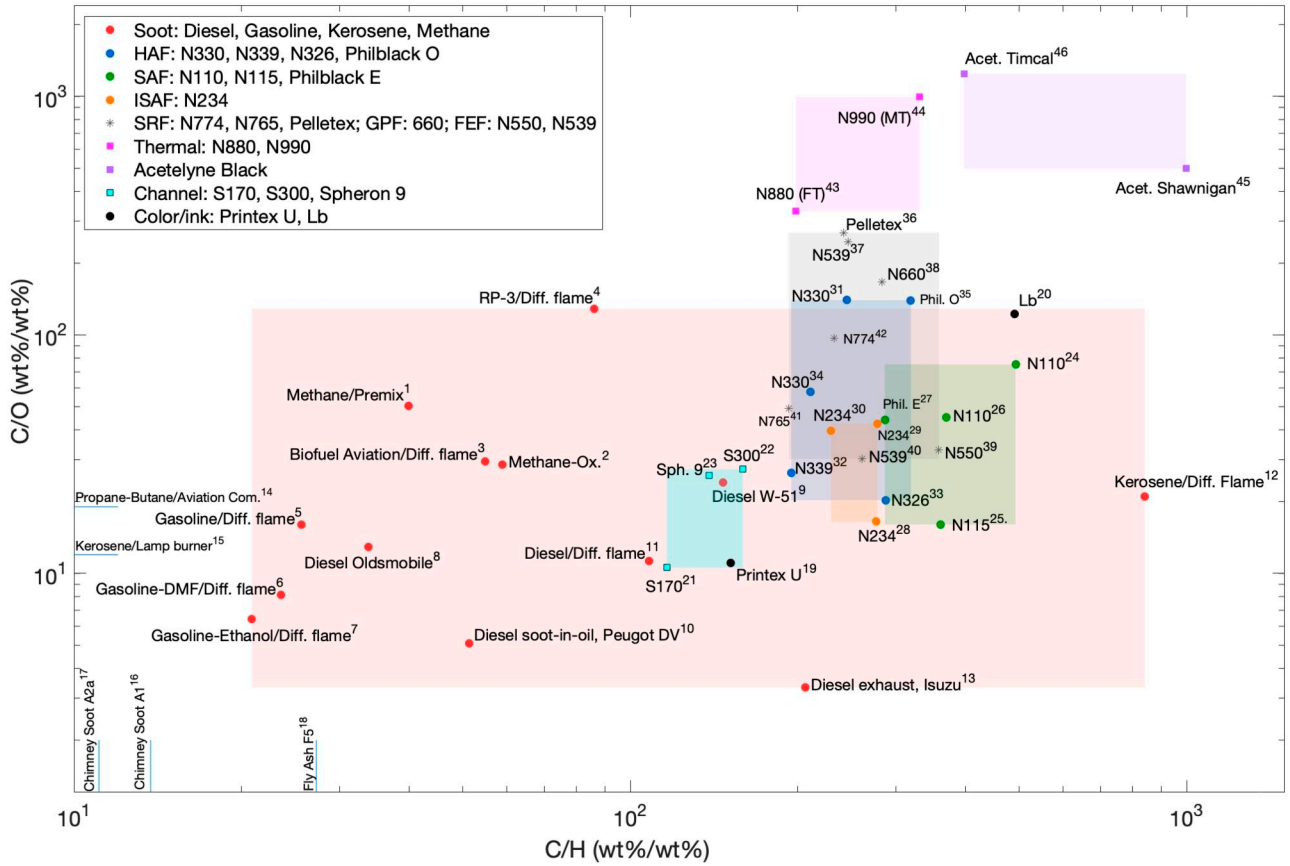

Figure 1. Soot and carbon black composition diagram. Superscript numbers on each data point correspond to the numbered entries in Table 2 where further details can be found regarding the samples, including references.

Table 1. Summary of soot and carbon black properties (Dannenberg 1978; Kim et al. 2009; ASTM Standards 2016).

Group	C/H (wt%/wt%)	C/O (wt%/wt%)	Typical d_p (nm)	Typical specific surface area (BET N_2 m^2g^{-1})
Soot	11.1–840	3.3–128.7	10–50	100–450
HAF (high abrasion furnace black)	192.6–319.3	20.3–139.9	30–39	70–99
SAF (super abrasion furnace black)	286.6–492.5	16.0–75.2	10–19	121–150
ISAF (intermediate super abrasion furnace black)	229.5–278.0	16.5–42.4	20–29	100–120
SRF, GPF, FEF (semi reinforcing, general purpose, and fast extrusion furnace black)	192.7–358.5	30.2–268.2	51–79	32–49
Thermal black	198.4–331.0	330.7–993.0	81–99	10–20
Acetylene black	398.0–997.0	498–1243.6	~40	72–1014
Channel black	116.2–159.3	10.6–27.3	10–39	80–115

and primary particle diameter of the final product. Such data is not common in the literature, because manufacturers rarely publish the conditions that produce any given carbon black product.

Van Niekerk (1994) closely studied the oil furnace black process producing a range of abrasion furnace blacks *via* a coupled CFD-soot simulation of an entire furnace black reactor. He had access to data from the Philips petroleum co. and produced a series of residence times and reactor temperatures corresponding to various reactor simulations focussing on the desired grades of furnace black. Furthermore, Donnet, Bansal, and Wang (1993) provided approximate reactor conditions as part of the "Carbon Black" textbook. In total, seven sets of reactor conditions were found in these sources, making up the data set that will be used to derive the model for the soot fusing timescale. It should be noted that no reactor conditions relating to channel black could be found possibly due to the significantly lower market share of this product.

The chosen reactor data were grouped into two sets. The first set includes all seven data points across the three abrasion furnace blacks (SAF + ISAF + HAF) and will be denoted as the *furnace black B model*. It represents a broad average of all available data that met the aforementioned criteria. The second set includes four data points comprising the SAF and ISAF grades,

Table 2. Further details and references regarding the data points in Figure 1.

	Carbonaceous sample	Manufacturer	C/H (wt. %/wt. %)	C/O (wt. %/wt. %)	Source
1.	Methane/Premix	–	39.96	50.47	Neoh 1980
2.	Methane-Ox.	–	58.88	28.55	Neoh 1980
3.	Biofuel Aviation/Diff. flame	–	54.85	29.43	Chang et al. 2022
4.	RP-3/Diff. flame	–	86.04	128.71	Chang et al. 2022
5.	Gasoline/Diff. flame	–	25.65	16.01	Guerrero Peña et al. 2018
6.	Gasoline-DMF/Diff. flame	–	23.57	8.12	Guerrero Peña et al. 2018
7.	Gasoline-Ethanol/Diff. flame	–	20.87	6.41	Guerrero Peña et al. 2018
8.	Diesel Oldsmobile	–	33.78	12.87	Ross et al. 1982
9.	Diesel W-51	–	146.69	24.02	Ross et al. 1982
10.	Diesel soot-in-oil, Peugot DV	–	51.37	5.09	Ferraro et al. 2016
11.	Diesel/Diff. flame	–	108.00	11.25	Daly and Horn 2009
12.	Kerosene/Diff. flame	–	840.00	21.00	Daly and Horn 2009
13.	Diesel exhaust, Isuzu	–	206.08	3.33	Bredin, Larcher, and Mullins 2011
14.	Propane-Butane/Aviation com.	–	–	19.00	Popovicheva et al. 2003
15.	Kerosene/Lamp burner	–	–	11.97	Popovicheva et al. 2003
16.	Chimney soot A1	–	13.73	–	Medalia, Rivin, and Sanders 1983
17.	Chimney soot A2a	–	11.09	–	Medalia, Rivin, and Sanders 1983
18.	Fly Ash F5	–	27.26	–	Medalia, Rivin, and Sanders 1983
19.	Printex U	Degussa AG	151.67	11.09	Nejar, Makkee, and Illangomez 2007
20.	Lb	–	490.00	122.50	Dannenberg 1978
21.	S170	Degussa Italia	116.22	10.58	Ferraro et al. 2016
22.	S300	Cabot Corp.	159.33	27.31	Dannenberg 1978
23.	Spheron 9	Cabot Corp.	138.55	25.77	Studebaker et al. 1956
24.	N110	Cabot Corp. CORAX	492.45	75.18	Ferraro et al. 2016
25.	N115	Cabot Corp. CORAX	360.88	16.04	Ferraro et al. 2016
26.	N110	Cabot Corp.	369.30	45.08	Risby and Sehnert 1988
27.	Philblack E	Phillips Chemical Co.	286.62	44.10	Studebaker et al. 1956
28.	N234	Cabot Corp. CORAX	276.35	16.48	Ferraro et al. 2016
29.	N234	Not given	278.04	42.40	Robertson and Hardman 2021
30.	N234	Shandong Lianke	229.48	39.66	Quan et al. 2018
31.	N330	Cabot Corp.	244.75	139.86	Dannenberg 1978
32.	N339	Cabot Corp.	194.61	26.42	Risby and Sehnert 1988
33.	N326	Cabot Corp. CORAX	287.85	20.30	Ferraro et al. 2016
34.	N330	Shandong Lianke	210.85	57.73	Quan et al. 2018
35.	Philback O	Phillips Chemical co.	319.29	139.41	Studebaker et al. 1956
36.	Pelletex	Phillips Chemical co.	242.00	268.16	Studebaker et al. 1956
37.	N539	Columbian Chemicals	246.5	246.5	Darmstadt, Roy, and Kaliaguine 1995
38.	N660	Not given	282.89	166.49	Robertson and Hardman 2021
39.	N550	Cabot Corp. CORAX	358.48	32.92	Ferraro et al. 2016
40.	N539	Cabot Corp. CORAX	260.65	30.23	Ferraro et al. 2016
41.	N765	Cabot Corp.	192.70	49.16	Risby and Sehnert 1988
42.	N774	Shandong Lianke	232.52	96.69	Quan et al. 2018
43.	N880	Cabot Corp.	198.40	330.67	Dannenberg 1978
44.	N990	Cabot Corp.	331.00	993.00	Dannenberg 1978
45.	Acet. Shawnigan	Cabot Corp.	997.00	498.50	Dannenberg 1978
46.	Acet. Timcal	Timcal Ltd.	397.96	1243.63	Quan et al. 2018

Table 3. Selected furnace black reactor data.

Carbon black grade		d_p (nm)	Reactor temperature (K)	Residence time (ms)	Source
N110	(SAF)	22	2050	8	Donnet, Bansal, and Wang 1993
N110	(SAF)	18	2126	7	Van Niekerk 1994
N100 series	(SAF)	18	2070	8	Van Niekerk 1994
N220	(ISAF)	21	1946	9.5	Van Niekerk 1994
N330	(HAF)	38	1820	31	Donnet, Bansal, and Wang 1993
N330	(HAF)	30	1804	25	Van Niekerk 1994
N300 series	(HAF)	30	1820	30	Van Niekerk 1994

whose composition is more similar to soot than HAF in terms of the C/O ratio. This will be denoted as the *furnace black A model*. Note how the SAF and ISAF shaded areas are fully contained within the soot red shaded area in Figure 1) and should behave as a proxy for a more oxygenated type of soot rather than a broad average. The selection of furnace blacks and corresponding reactor data is shown in Table 3.

4. Derivation of soot fusing model with inverse population balance

4.1. The furnace black reactor

Before showing the derivation of the fusing model from the furnace black reactor data, we first provide an overview of this process and explain the key assumptions to be made in its analysis (Figure 2).

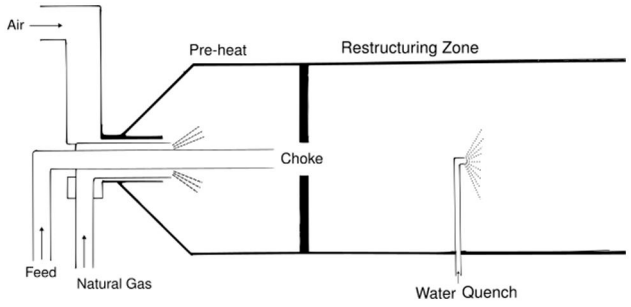

Figure 2. Schematic of the furnace black process.

The first stage of the reactor is called the *pre-heat*. Commonly natural gas and air is burnt to heat the reactor to a temperature of over 2000 K in preparation for the feed to be injected into the flow. It is assumed that all the oxygen and natural gas is consumed before the feed is injected, as excess oxygen would oxidize and consume any carbon black particles made. Second, the feed is injected usually as a spray toward the narrowing section of the reactor known as *the choke*, where it is instantaneously pyrolized, producing a cloud of small spherical carbonaceous nuclei. Due to the elevated temperatures through the choke where this conversion process takes place, nucleation and surface growth rates are extremely fast, rapidly consuming the feed.

Based on the above, it is assumed that the feed is consumed entirely and the cloud of small nuclei particles enters the restructuring zone in an oxygen and feed starved environment. Essentially, once the nuclei have passed through the choke, it is assumed that surface growth and oxidation do not play a role due to the lack of the gas-phase species needed for them to occur. Shortly after the choke, a quench is applied to cool the nuclei to the appropriate temperature for the restructuring process to begin.

Insight from Wang et al. (2003) suggests that nucleation accounts for 10% of the conversion process while surface growth accounts for 90%. Essentially, if nuclei are of order 1 nm in diameter, surface growth leads to a 10-fold increase in particle volume (Diemer 2023). The resulting larger spherical nuclei would have a diameter of 2.15 nm at the end of the conversion process, which is assumed to be terminated at the quench plane. The assumption of 10/90 split between nucleation and growth could have an effect on the initial primary particle size subsequently used. However, the initial primary size was found to have low sensitivity to the nucleation/growth conversion split assumption. For example, a 95% growth—5% nucleation split produces a primary particle size of 2.71 nm. Subsequent fusing model parameters, such as activation temperature and primary particle diameter scaling were found to also be relatively insensitive to the assumed split between growth and nucleation in the conversion step. This sensitivity analysis is provided in Appendix A. Since the final primary particle size of furnace black range from 20 to 70 nm, it can be seen that the conversion and restructuring processes are effectively decoupled. The large nuclei of 2.15 nm produced by complete conversion, with a total number density of $\mathcal{O}(10^{23})$ particles/gmol of carrier gas, can be considered as initial conditions for the subsequent restructuring process (Diemer 2023).

The restructuring zone is governed by the competing processes of collision and fusing. By controlling the residence time and temperature of the restructuring zone, different morphologies of the final product can be achieved. If the collision or aggregation rate is faster than the fusing of primary particles within aggregates, then open, fractal aggregates with smaller primary particles will be produced. If the fusing process is far faster than the collision process, then more compact aggregates will be formed with larger primary particles. To avoid further heat input, the restructuring zone is insulated and can be viewed as an isothermal plug flow reactor. Thus, using an approach similar to that of Diemer (2023) and the monodisperse model of Kruis et al. (1993), the restructuring process can be simplified such that only knowledge of the reactor temperature, final primary particle size, and residence time are needed to derive the model for the characteristic fusing time, as will be shown in the next section.

4.2. Calculation of fusing timescales from reactor data

In the following, an inverse population balance approach will be adopted to derive an expression for the fusing timescale. The procedure is similar to that of Diemer (2023), where more details can be found (Section 4).

It must first be noted that, when considering the reactor data available, only average quantities describing the particulate phase can be found; namely, the average primary particle diameter across all aggregates. This permits the use of an appropriately simplified population balance approach that utilizes only the available information. Such a formulation is the monodisperse model of Kruis et al. (1993), which accounts for the average effect of fusing on the surface area of aggregates and has been employed for the

kinetics of inorganic nanoparticles in cases where aggregation and sintering are the only processes present. This situation describes well the case of the furnace black restructuring zone and, therefore, this model is appropriate for the extraction of the fusing timescale from data in that zone. It is important to stress that the fusing timescale expression derived from this procedure can subsequently be used with any detailed population balance approach that includes the fusing of aggregates. For example, a more advanced two-PBE approach, such as the one employed in Sun, Rigopoulos, and Liu (2021) includes the effect of fusing on the underlying primary particle distribution itself and processes, such as surface growth and oxidation. However, the fusing timescale is a kinetic parameter, hence not anchored to any particular population balance formulation; it can thus be used in conjunction with the aforementioned two-PBE approach to describe, e.g., soot formation in flames where more kinetic processes are present.

We now describe the inverse population balance approach based on the model of Kruis et al. (1993). For the purpose of this analysis, aggregates will be described by their volume, V, and surface area, A. Furthermore, since we will be using a monodisperse model, all aggregates are described by a mean size and surface area, V_n and A_n, respectively. We will employ a plug flow reactor model assuming a constant axial velocity, u_z, and define a time variable, $\tilde{t}$, as follows:

$$\tilde{t} = \frac{z}{u_z} \tag{8}$$

Fusing does not change the volume fraction of aggregates (M_1) or the total number of aggregates (M_0). Thus the first moment is a constant, and the evolution of the zeroth moment is only a function of the Brownian collision between aggregates, $M_0(\tilde{t})$:

$$\frac{dM_0}{d\tilde{t}} = -\frac{\beta(T)}{2} M_0^2 \tag{9}$$

$$\frac{dM_1}{d\tilde{t}} = 0 \tag{10}$$

The evolution of the mean volume $V_n(\tilde{t}\ )$, is given by the ratio on the first moment to zeroth moment:

$$\frac{dV_n}{d\tilde{t}} = \frac{\beta(T)}{2} M_1 \tag{11}$$

In the above, $\beta(T)$ is the collision frequency function. Carbon black aggregates in the restructuring zone are considered to be large enough to aggregate according to the Brownian collision mechanism and $\beta(T)$ is thus given by:

$$\beta(T) = \frac{8 k_B T}{3 \mu_g} \tag{12}$$

where μ_g is the viscosity of the gas.

The model of Kruis et al. (1993) also accounts for the evolution of the mean surface area of aggregates ($A_n(\tilde{t}\ )$) due to collision and fusing within the monodisperse framework:

$$\frac{dA_n}{d\tilde{t}} = \underbrace{\frac{A_n}{V_n}\frac{dV_n}{d\tilde{t}}}_{\text{collision}} \underbrace{- \frac{1}{\tau_\sigma}(A_n - A_s)}_{\text{fusing}} \tag{13}$$

where A_s is the spherical equivalent surface area of an aggregate.

It is convenient to define some non-dimensional ratios and to non-dimensionalize Equation (13), and this procedure will highlight how to determine a characteristic fusing time for a given set of reactor conditions and final primary particle size. We thus define a scaled residence time, ξ, and a normalized surface area, $\tilde{\mathrm{A}}_\mathrm{n}$, based on the initial zeroth moment and surface area ($M_0(0)$ and $A_n(0)$, respectively) as follows:

$$\xi = \frac{\tilde{t}}{\tau_\beta} \tag{14}$$

$$\tilde{\mathrm{A}}_\mathrm{n} = \frac{A_n(\tilde{t})}{A_n(0)} \tag{15}$$

To define a characteristic collision timescale, the right hand-side of Equation (9) can be shown to be the product of a quantity with units of reciprocal time and number density. When evaluated at the initial conditions, this defines the maximum characteristic collision rate and hence the corresponding collision timescale, to be denoted by t_β:

$$\frac{dM_0}{d\tilde{t}} = -\frac{1}{\tau_\beta} M_0 \tag{16}$$

$$\tau_\beta = \frac{2}{\beta(T) M_0(0)} \tag{17}$$

Furthermore, Equation (13) can be non-dimensionalized as follows, to describe the evolution of non-dimensional surface area $\tilde{\mathrm{A}}(\xi)$:

$$\frac{d\tilde{\mathrm{A}}_\mathrm{n}}{d\xi} = \frac{\tilde{\mathrm{A}}_\mathrm{n}}{1+\xi} - \frac{\tau_\beta}{\tau_\sigma}\left[\tilde{\mathrm{A}}_\mathrm{n} - (1+\xi)^{\frac{2}{3}}\right] \tag{18}$$

Equation (11) can also be expressed in terms of ξ and an initial aggregate volume $V_n(0)$:

$$V_n(\xi) = V_n(0)(1+\xi) \tag{19}$$

When the fusing timescale is very long relative to the collision timescale, the second term on the right-

hand side of Equation (18) becomes negligible, and only the collision process affects the evolution of aggregate surface area. Equation (18) can be solved to find the fusing timescale given the initial conditions and reactor data. We now consider a ratio of primary particle sizes, where the primary particle size is defined as $d_p = 6V_n/A_n$, between an initial state $d_0 = 6V_n(0)/A_n(0)$ and an evolved primary particle size $d_p(\xi)$:

$$\frac{d_p(\xi)}{d_0} = \frac{V_n(0)(1+\xi)}{V_n(0)} \frac{A_n(0)}{A_n(\xi)} \tag{20}$$

Finally, using the relations presented in Equations (15), (18), and (19)—the following equation can be used to predict the relative change in primary particle size:

$$\frac{d_p(\xi)}{d_0} = \frac{1+\xi}{\tilde{A}_n(\xi)} \tag{21}$$

where d_p is an average primary particle diameter assuming that all primary particles within a single aggregate are the same size, and d_0 is the initial primary particle diameter.

The procedure for obtaining the fusing timescale is as follows. An initial guess for it is first introduced into Equation (18), which is solved numerically. Next, using Equation (21), the resulting primary particle size is calculated and compared to known furnace black primary particle sizes. The initial guess for fusing timescale is updated and improved iteratively until the predicted value of d_p converges to the known furnace black primary particle diameter. This procedure is repeated for all of the selected furnace black grades.

4.3. Determination of scaling law for the fusing timescale

The inverse population balance approach will now be employed to determine the appropriate form of the scaling law for the fusing timescale.

First, the temperature dependence of the timescale can be inferred, given that this dependence for solid-state diffusion coefficients and viscosity is commonly expressed *via* Arrhenius laws. Thus, an Arrhenius law should produce a linear relationship between the natural logarithm of the fusing timescale and the inverse temperature. Figures 3a and b confirm this relationship. Thus the temperature can be assumed to be proportional to $\exp(T_a/T)$, where T_a is the activation temperature.

Second, it is possible to infer the dependence of the fusing timescale on primary particle diameter by considering a range of scaling relationships already present in initial stage neck growth models. Coblenz et al. (1980) reviewed numerous neck growth fusing expressions and, after one characteristic fusing timescale has elapsed, all of them assume the following general form (Diemer 2023):

$$\frac{d_p^m}{\tau_\sigma} = Kf(T) \tag{22}$$

where K is a constant unique to a specific fusing mechanism, $f(T)$ is an increasing function of temperature and m takes positive integer values for each potential fusing mechanism. As an example, the surface diffusion model (Coblenz et al. 1980) in its original form is shown below:

$$\left[\frac{x(t)}{d_p}\right]^5 = \left[\frac{225}{2RT}\frac{\delta D_s(T)\Omega(T)\gamma_{sv}(T)}{d_p^4}\right]t \tag{23}$$

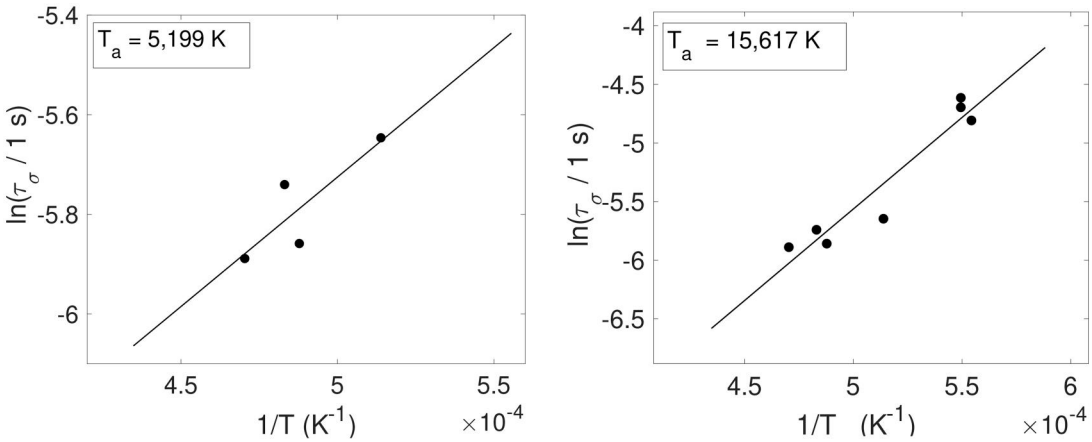

(a) Furnace black A (SAF + ISAF). (b) Furnace black B (SAF + ISAF + HAF).

Figure 3. Relationship of $\ln \tau_\sigma$ with $1/T$ for both furnace black models.

where $x(t)$ is the neck size between two spherical particles, d_p is the particle diameter, δ is a surface thickness length-scale, D_s is the diffusivity, γ_{sv} is the surface energy and Ω is the molar volume. If we express the characteristic neck size expressed as a proportion of the particle diameter, i.e., $x(\tau_\sigma) = \epsilon d_p$, Equation (23) can be rewritten in the form of Equation (22):

$$\frac{d_p^4}{\tau_\sigma} = \frac{225}{2\epsilon^5} \underbrace{\frac{\delta D_s(T)\Omega(T)\gamma_{sv}(T)}{RT}}_{f(T)} \tag{24}$$

For a plausible scaling relationship to be found, $f(T)$ must be an increasing function of T, as this respects the underlying theory that hotter particles fuse faster. An increasing function with temperature can equivalently be viewed as a decreasing function with inverse temperature: $1/T$. To demonstrate this, consider a general form of the fusing timescale expression with an unknown primary particle scaling parameter m:

$$\tau_\sigma \propto d_p^m \ \exp\left(\frac{T_a}{T}\right) \tag{25}$$

Rearranging for the required ratio as shown in Equation (22):

$$\frac{d_p^m}{\tau_\sigma} \propto \ \exp\left(\frac{-T_a}{T}\right) \tag{26}$$

Hence the negative slope with 1/T appears:

$$\log\left(\frac{d_p^m}{\tau_\sigma}\right) \propto \ \frac{-T_a}{T} \tag{27}$$

Consequently, given sufficient experimental data, a scaling relationship with respect to primary particle size can be inferred by plotting curves of d_p^m/τ_σ for a range of values of m (the exponent in Equation (22)) against inverse temperature. The curve with a negative slope can be considered as a plausible scaling relationship. Figure 4, presents this analysis, and $m = 1$ is shown to be the only plausible scaling relationship.

Although the viscous flow mechanism features $m = 1$, it should be stressed that the outcome of this analysis does not imply this particular physical mechanism, since more than one mechanism can feature the same scaling relationship. All that can be concluded from Figure 4 is that a linear scaling relationship is the only plausible relationship, based on the furnace black reactor data previously compiled. The fusing expression can now be written as follows:

$$\tau_\sigma \propto d_p \exp\left(\frac{T_a}{T}\right) \tag{28}$$

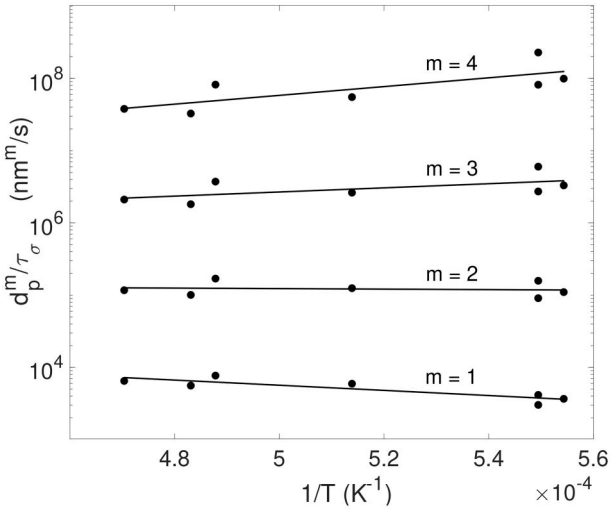

Figure 4. Proposed primary particle scaling relationships regarding the fusing timescale. A negative gradient implies a plausible scaling relationship.

The final step is to determine the pre-exponential factor. This can be achieved by rearranging Equation (28) into the following form:

$$\frac{\tau_\sigma}{d_p \exp\left(\frac{T_a}{T}\right)} = A_0 \tag{29}$$

where A_0 is the pre-exponential factor. Using the available data points, the values for A_0 can be determined from Figures 3a and b. The final expressions for the fusing timescale are given below:

Furnace black A model:

$$\tau_\sigma = (1.2 \times 10^4) d_p \exp\left(\frac{5,199}{T}\right) \tag{30}$$

Furnace black B model:

$$\tau_\sigma = (66.7) \ d_p \exp\left(\frac{15,617}{T}\right) \tag{31}$$

5. Simulation of the inert reheating experiment of Ono et al. (2017)

5.1. Description of experiment

In the present section, the new fusing models will be applied to the simulation of the experiment of Ono et al. (2017). The experimental setup consists of two separate reaction tubes with a particulate filter in between. The first reaction tube is used to generate the soot aggregates at various temperatures, resulting in a range of aggregate sizes. Next, a particle neutralizer and Differential Mobility Analyzer (DMA)

instrument is used to filter the aggregates by mobility diameter, with only one chosen diameter being able to pass though into the second reaction tube where reheating takes place. When the soot aggregates are sampled from the first reaction tube, an abundance of nitrogen gas is used to create an inert environment, as well as to dilute the total number density of aggregates, effectively ensuring that no more collisions occur.

The second reaction tube applies a known temperature distribution to the aggregates and the resultant decrease in mobility diameter is recorded at the outlet. Thus, when considering the second reaction tube alone, a monodisperse initial condition is created *via* the use of the particle neutralizer and DMA device, and inert reheating of a dilute aggregate sample isolates the effect fusing. It is fusing alone that causes the reduction in mobility diameter and the associated reduction in surface area of aggregates. This experiment to the author's knowledge is only soot fusing experiment that isolates the fusing behavior alone and serves as an ideal validation case for any soot fusing timescale expression.

Mobility diameters at the inlet and outlet of the reheating tube have been measured. However, only inlet primary particle diameters have been shown for aggregates of 180 nm in mobility diameter, and these results will be focus in the present work. Furthermore, two fuels are used to generate soot in the first reaction tube at different temperatures, namely ethylene-derived soot (generated at 1600 and 1800 K) and benzene-derived soot (at 1500 and 1700 K).

5.2. Particle size relations for fractal aggregates

The average primary particle diameter of an aggregate can be estimated *via* the volume-to-surface area relation, as shown below:

$$d_p = \frac{6v}{a} \tag{32}$$

where v is the volume of an aggregate, a is the surface area of an aggregate and d_p is the average primary particle size. For aggregates undergoing fusing alone, the volume of the aggregate as a whole remains constant. Considering an aggregate at two states, the corresponding ratio of primary particle sizes is given by:

$$\frac{d_{p,2}}{d_{p,1}} = \frac{a_1}{a_2} \tag{33}$$

Moreover, the following equation relates the mobility diameter to the corresponding primary particle diameter:

$$d_p = \left[\frac{\pi k_a}{6v}(d_m)^{2D_\alpha}\right]^{1/(2D_\alpha-3)} \tag{34}$$

Where D_α and k_α are fractal parameters extracted from experiment or numerical studies. This expression has been shown to be valid for numerous fusing mechanisms with an average value of D_α being used (Eggersdorfer et al. 2012). The fusing throughout the second reactor is assumed to occur with a constant fractal dimension, with aggregates initially assuming a known mass fractal dimension of 1.8 for combustion generated soot. Although the exact initial fractal dimension was not measured directly by Ono et al. (2017), there is significant evidence confirming this feature of combustion generated soot (Link et al. 2011). Finally, the ratio of aggregate surface area at two states can be related to the ratio of mobility diameters as follows:

$$\frac{d_{m,2}}{d_{m,1}} = \left(\frac{a_2}{a_1}\right)^{\frac{3-2D_\alpha}{2D_\alpha}} \tag{35}$$

5.3. Plug-flow reactor model

Equation (1) can be solved analytically and then applied piece-wise across the 11 sections of the plug-flow reactor model, where each section corresponds to an axial temperature measurement presented in the recent work of Matsukawa et al. (2023). A nominal flow rate at standard conditions was stated by Ono et al. (2017) and has been scaled with increasing temperature at constant pressure. By accounting for varying volumetric flow rate and the geometry of each plug-flow section, a corresponding residence time, Δt_i, can be calculated for each section i. Therefore, the following equation represents the evolution of normalized surface area $\alpha = a/a_0$, across an individual section ΔL_i at temperature T_i:

$$\alpha_i = \alpha_{i-1}\exp\left(\frac{-\Delta t_i}{\tau_\sigma(T_i)}\right) + a^*\left[1 - \exp\left(\frac{\Delta t_i}{\tau_\sigma(T_i)}\right)\right] \tag{36}$$

where a^* is the normalized spherical equivalent area, i.e., $a^* = a_s/a_0$, τ_σ is the fusing timescale evaluated at local conditions and α_i is the normalized surface area at the outlet of each section. Note that, at the inlet, $\alpha_0 = 1$. The model described by Equation (36) is shown schematically in Figure 5. Eleven sections are used due to the availability of axial temperature measurements. Equation (36) produces a prediction of outlet normalized surface area, which can then be

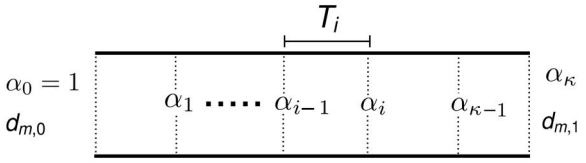

Figure 5. Schematic of plug-flow reactor model used to simulate the inert reheating experiment of Ono et al. (2017).

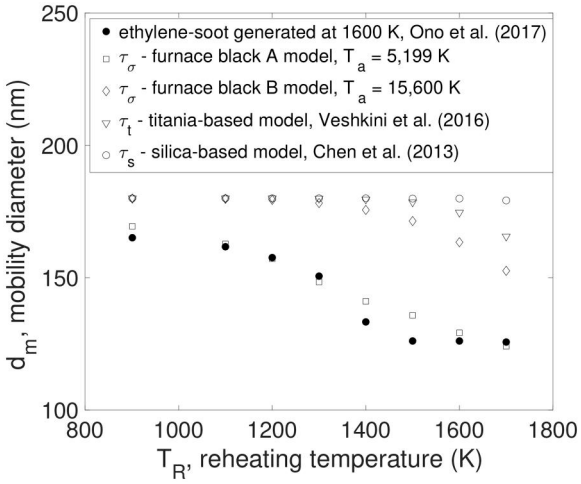

Figure 6. Final reduced mobility diameter $d_{m.1}$ of aggregates due to fusing. Soot sample prepared using ethylene at 1600 K.

converted into a mobility diameter prediction *via* Equation (35).

5.4. Results and discussion

All of the experiments were simulated using the new models (Equations (30) and (31)), as well as the fusing timescales of Veshkini, Dworkin, and Thomson (2016) (Equation (5)) and Chen et al. (2013) (Equation (6)). The predicted mobility diameters will now be compared with the experimentally measured ones. Note that the reheating temperature shown is a representative maximum reactor temperature whereas the full axial temperature distribution for each test case is reproduced from Matsukawa et al. (2023).

Figure 6 shows results for the ethylene-derived soot generated at 1600 K. The furnace black A model, derived from the more oxygenated subset of furnace black grades, has the closest agreement with experimental results across all reheat temperatures for ethylene-derived soot generated at 1600 K, as shown in Figure 6. Furthermore, this model has an average error of 3% with a maximum error at 1500 K reheat temperature of 8%. This is much better than the average errors of over 25% for the previous titania-based and silica-based fusing timescales. The less oxygenated furnace black B fusing timescale performs similarly to

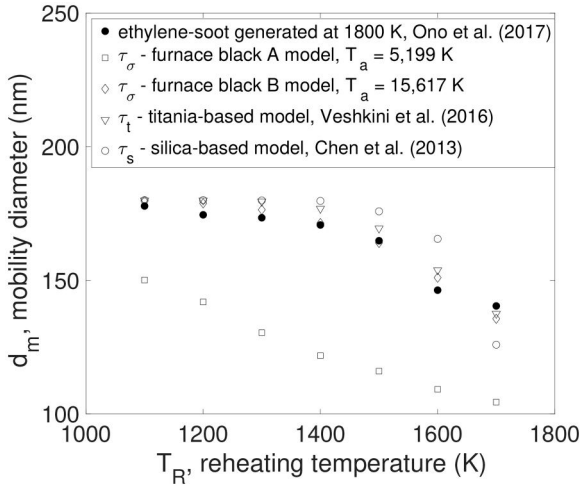

Figure 7. Final reduced mobility diameter $d_{m.1}$ of aggregates due to fusing. Soot sample prepared using ethylene at 1800 K.

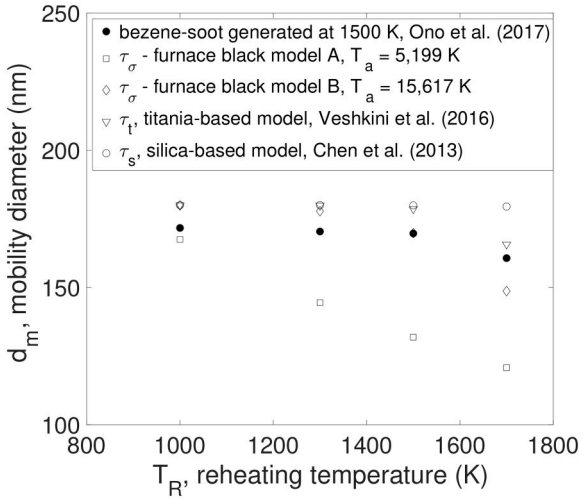

Figure 8. Final reduced mobility diameter $d_{m.1}$ of aggregates due to fusing. Soot sample prepared using benzene at 1500 K.

the titania-based and silica-based models, and overall these three models do not capture well the fusing behavior in this experiment.

The experiment with ethylene-derived soot produced at 1800 K was then simulated, and Figure 7 shows the mobility diameter predictions. Here, it is the furnace black B fusing timescale that most faithfully predicts the decrease in mobility diameter due to reheating with an average error of 2%. However, the titania-based and silica-based fusing timescales also perform well, with average errors of 3 and 6%, respectively. It is the more oxygenated furnace black A model that significantly overpredicts the extent of fusing across all reheating temperatures.

Figures 8 and 9 show the mobility diameter predictions for benzene-derived soot generated at 1500 and 1700 K, respectively. The furnace black B model

performs best across both benzene-derived soot cases, with average errors of 4 and 3%, respectively. The titania-based model performs well and successfully captures the fusing behavior of benzene-derived soot, with average errors of 5 and 7%, respectively. The furnace black A model consistently overpredicts the extent of fusing in the benzene-derived soot cases and significantly underpredicts the final mobility diameters with average errors of 16 and 20%, respectively. Finally, the silica-based model performs poorly in both benzene-derived soot cases and struggles to predict any fusing behavior at all at the highest reheat temperatures.

The average error of each fusing timescale model, for each soot sample has been summarized in Table 4. The furnace black A model performed best in the ethylene prepared at 1600 K case while the furnace black B model performed best in the other three test cases. Overall, the furnace black models provide a better prediction than the expressions based on silica and titania expressions, if one selects the right furnace black model for each case. The right choice of furnace black model can be rationalized based on the composition of the samples that were employed for the derivation of each model, as discussed below. By contrast, the level of agreement of the models extrapolated from titania and silica has no rational basis.

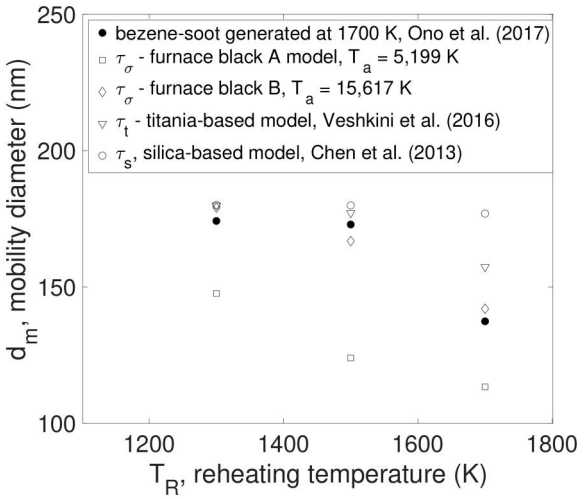

Figure 9. Final reduced mobility diameter $d_{m,1}$ of aggregates due to fusing. Soot sample prepared using benzene at 1700 K.

Ono et al. (2017) showed evidence that the ethylene-derived soot samples had a higher quantity of aliphatic surface groups vs. the benzene-derived soot, which was almost entirely composed of aromatic compounds. The origin of the two furnace black fusing models reflects differences in oxygen content, which is found exclusively on the surface of soot primary particles, and the furnace black A model is derived from a more oxygenated subset of carbon black grades than the furnace black B model. Notably, the furnace black A model performed the best when predicting the fusing of ethylene-derived soot prepared at the lower temperature of 1600 K, whereas furnace black B successfully captured the fusing behavior of the ethylene-derived soot prepared at 1800 K and both benzene-derived soot samples. A qualitative link can be drawn between the surface composition of each soot sample and the observed fusing behavior. The reaction temperature at which soot particles are generated clearly has an important influence on the eventual composition and surface groups defining the primary particles, and this in turn determines which fusing activation temperature is most appropriate between the two fusing models derived from furnace black, as evidenced in the simulated results shown in the present section.

Finally, Matsukawa et al. (2023) reexamined the experimental results of Ono et al. (2017) and calculated fusing activation temperatures for the various soot samples studied. The fusing activation temperatures found were broadly consistent with the values and trends found in the present work with models based on furnace black reactor data. For example, Matsukawa et al. (2023) quote an fusing activation temperature of 12,072 K for ethylene-derived soot prepared at 1600 K and 16,850 K for ethylene-derived soot produced at 1800 K. Comparatively, the furnace black A model has an activation temperature of 5199 K, whilst the furnace black B has an activation temperature of 15,617 K. Conversely, the titania-based and silica-based models exhibit far higher activation temperatures of 33,100 and 100,000 K, respectively. For a given fuel, increasing the reaction temperature produces a higher fusing activation temperature associated with the resulting soot aggregates. This alludes

Table 4. Summary of average error in each fusing model.

Soot sample	Furnace black A	Furnace black B	Titania-based Veshkini, Dworkin, and Thomson (2016)	Silica-based Chen et al. (2013)
Ethylene prep. 1600 K	3%	21%	25%	27%
Ethylene prep. 1800 K	24%	2%	3%	6%
Benzene prep. 1500 K	16%	4%	5%	7%
Benzene prep. 1700 K	20%	3%	7%	12%

to fewer surface groups being formed and a different soot composition that in turn fuses slower. This trend is found in both the ethylene-derived and benzene-derived soot samples, as well as in the two models derived from furnace black.

It has been argued that the graphitic nature of soot, and particularly the formation of a hard graphitic shell in each primary particle, discounts the very presence of fusing due to a surface area minimization mechanism (Morgan, Patterson, and Kraft 2008; Balthasar and Frenklach 2005). Essentially, it is argued that soot is too solid or hard for fusing to occur at all. However, the experiments of Ono et al. (2017) and Matsukawa et al. (2023) provide evidence of soot aggregate fusing is possible, and an explanation of this apparent contradiction is possible. Every particulate process that is involved with the production and evolution of soot aggregates has an associated timescale that will in general depend on the local conditions: the gas-phase concentrations of relevant precursors, the temperature, and the particle number and size distribution. As mentioned earlier, the graphitic nature of any given soot aggregate and the surface groups present may vary widely. It is, therefore, plausible that, if the fusing activation temperature is sufficiently high, the associated fusing timescale may be far longer than the other simultaneously occurring processes. Namely, surface growth which dominates in high acetylene environments and is responsible for its own type of aggregate restructuring known as *obliteration* (Park and Rogak 2004) may be dominant compared to restructuring due to fusing. Comparing the timescales for surface growth and fusing will reveal whether each restructuring mechanism is necessary in a given case. However, in the absence of surface growth, the only available mechanism that accounts for the evolving morphology of aggregates is fusing, and the present work has identified the restructuring zone in the furnace black process as a valid source of experimental data to derive a soot fusing timescale expression.

6. Conclusions

By careful comparison between a wide variety of soot samples and carbon black grades, a selection of abrasion furnace blacks and channel blacks were deemed suitable for use as soot proxies in the context of aggregate fusing. Despite the limited availability of reactor data, seven sets of reactor conditions were found defining the residence time, reactor temperature, and primary particle diameter of N110 (SAF), N220 (ISAF), and N330 (HAF) furnace black grades. Two models for the characteristic fusing timescale were subsequently derived from this data. A linear relationship between the fusing timescale and primary particle diameter was found as most feasible. An activation temperature of 15,617 K was obtained for the fusing model derived from all three furnace black grades (less oxygenated), while an activation temperature of 5,199 K was found for the fusing model determined from the more oxygenated subset of just SAF and ISAF grades (more oxygenated).

The inert reheating experiment of Ono et al. (2017) was simulated and the results compared against experiment data for reduced mobility diameter across four soot samples: (1) ethylene-derived soot prepared at 1600 K, (2) ethylene-derived soot prepared at 1800 K, (3) benzene-derived soot prepared at 1500 K, and (4) benzene-derived soot prepared at 1700 K. Two models previously used in the literature of sooting flame simulations, based on titania and silica, were also employed for comparison. The more oxygenated furnace black model performed best across all reheating temperatures involving soot sample 1 with an average error of 3%, while the less oxygenated furnace black model produced better predictions for soot sample 2 with an average error of 2%. When considering soot samples 3 and 4, the less oxygenated furnace black model performs best with average errors of 4 and 3%, respectively. The titania- and silica-based models performed well in some cases and not so well in others—notably, they both failed to predict the right fusing behavior in sample 1.

The differences in the performance of the two models can be explained based on the surface composition of each soot sample and the oxygen content of furnace blacks employed for the derivation of the fusing models. The fusing of the lower temperature ethylene-derived soot sample is best captured by the lower activation temperature (5,199 K) furnace black model, whilst the fusing of the higher temperature ethylene-derived soot sample and both benzene-derived soot samples are more closely described by the furnace black fusing model with higher activation temperature of 15,617 K. A comparison of the activation temperatures in the two furnace-black-derived models with those obtained by Matsukawa et al. (2023) from the experimental data of the Ono et al. (2017) experiment showed also that the trends are consistent.

Overall, the furnace-black-derived models successfully captured the features of the experiment. The present work demonstrates that certain grades of carbon

black can be used as a soot proxy material to derive a more realistic fusing timescale than previously used in soot models. Future work will employ these fusing models for detailed simulations of sooting flames.

Disclosure statement

No potential conflict of interest was reported by the author(s).

Funding

Daniel O'Sullivan gratefully acknowledges the financial support by the Engineering and Physical Sciences Research Council (EPSRC) in the form of a Doctoral Training Partnership (DTP).

References

Adachi, K., S. H. Chung, and P. R. Buseck. 2010. Shapes of soot aerosol particles and implications for their effects on climate. *J. Geophys. Res.* 115 (D15):15206. doi: 10.1029/2009JD012868.

ASTM Standards. 2016. *Standard classification system for carbon blacks used in rubber products*. West Conshohocken, PA: ASTM International.

Balthasar, M., and M. Frenklach. 2005. Monte-Carlo simulation of soot particle coagulation and aggregation: The effect of a realistic size distribution. *Proc. Combust. Inst.* 30 (1):1467–75. doi: 10.1016/j.proci.2004.07.035.

Boger, T., D. Rose, P. Nicolin, N. Gunasekaran, and T. Glasson. 2015. Oxidation of soot (Printex® U) in particulate filters operated on gasoline engines. *Emiss. Control Sci. Technol.* 1 (1):49–63. doi: 10.1007/s40825-015-0011-1.

Bond, T. C., and R. W. Bergstrom. 2006. Light absorption by carbonaceous particles: An investigative review. *Aerosol Sci. Technol.* 40 (1):27–67. doi: 10.1080/02786820500421521.

Bond, T. C., S. J. Doherty, D. W. Fahey, P. M. Forster, T. Berntsen, B. J. Deangelo, M. G. Flanner, S. Ghan, B. Kärcher, D. Koch, et al. 2013. Bounding the role of black carbon in the climate system: A scientific assessment. *JGR Atmos.* 118 (11):5380–552. doi: 10.1002/jgrd.50171.

Bredin, A., A. V. Larcher, and B. J. Mullins. 2011. Thermogravimetric analysis of carbon black and engine soot—Towards a more robust oil analysis method. *Tribol. Int.* 44 (12):1642–50. doi: 10.1016/j.triboint.2011.06.002.

Broday, D. M., and R. Rosenzweig. 2011. Deposition of fractal-like soot aggregates in the human respiratory tract. *J. Aerosol Sci.* 42 (6):372–86. doi: 10.1016/j.jaerosci.2011.03.001.

Chandrasekhar, S. 1961. *Hydrodynamic and hydromagnetic stability*. New York, NY: Dover.

Chang, D., J. Li, Y. Yang, and Z. Gan. 2022. Soot morphology and nanostructure differences between Chinese aviation kerosene and algae-based aviation biofuel in free jet laminar diffusion flames. *ACS Omega* 7 (14):11560–9. doi: 10.1021/acsomega.1c05125.

Chen, D., Z. Zainuddin, E. Yapp, J. Akroyd, S. Mosbach, and M. Kraft. 2013. A fully coupled simulation of PAH and soot growth with a population balance model. *Proc. Combust. Inst.* 34 (1):1827–35. doi: 10.1016/j.proci.2012.06.089.

Coblenz, W. S., W. M. Dynys, R. M. Cannon, and R. L. Coble. 1980. Initial stage solid state sintering models. *Sint. Process.* 13:141–57.

Daly, H. M., and A. B. Horn. 2009. Heterogeneous chemistry of toluene, kerosene and diesel soots. *Phys. Chem. Chem. Phys.* 11 (7):1069–76. doi: 10.1039/b815400g.

Dannenberg, E. 1978. Carbon black. In *Kirk-Othmer encyclopedia of chemical technology*. Vol. 4, 4th ed., 1037–74. New York, NY: John Wiley & Sons.

Darmstadt, H., C. Roy, and S. Kaliaguine. 1995. Characterization of pyrolytic carbon blacks from commercial tire pyrolysis plants. *Carbon* 33 (10):1449–55. doi: 10.1016/0008-6223(95)00096-V.

Diemer, R. B. 2023. Simplifying population balance models to promote broader use in industry. *Chem. Eng. Res. Des.* 190:91–105. doi: 10.1016/j.cherd.2022.12.002.

Donnet, J. B., R. Bansal, and M. Wang. 1993. *Carbon black: Science and technology*. 2nd ed. New York, NY: Marcel Dekker.

Eggersdorfer, M. L., D. Kadau, H. J. Herrmann, and S. E. Pratsinis. 2012. Aggregate morphology evolution by sintering: Number and diameter of primary particles. *J. Aerosol Sci.* 46:7–19. doi: 10.1016/j.jaerosci.2011.11.005.

Ferraro, G., E. Fratini, R. Rausa, P. Fiaschi, and P. Baglioni. 2016. Multiscale characterization of some commercial carbon blacks and diesel engine soot. *Energy Fuels* 30 (11):9859–66. doi: 10.1021/acs.energyfuels.6b01740.

Forestieri, S. D., T. M. Helgestad, A. T. Lambe, L. Renbaum-Wolff, D. A. Lack, P. Massoli, E. S. Cross, M. K. Dubey, C. Mazzoleni, J. S. Olfert, et al. 2018. Measurement and modeling of the multiwavelength optical properties of uncoated flame-generated soot. *Atmos. Chem. Phys.* 18 (16):12141–59. doi: 10.5194/acp-18-12141-2018.

Frenkel, J. 1945. Viscous flow of crystalline bodies under the of surface tension. *J. Phys.* 9 (5):385–91.

Friedlander, S. K., and M. K. Wu. 1994. Linear rate law for the decay of the excess surface area of a coalescing solid particle. *Phys. Rev. B Condens. Matter.* 49 (5):3622–4. doi: 10.1103/physrevb.49.3622.

German, R. M., and Z. A. Munir. 1976. Surface area reduction during isothermal sintering. *J. Am. Ceram. Soc.* 59 (9–10):379–83. doi: 10.1111/j.1151-2916.1976.tb09500.x.

Guerrero Peña, G. D., Y. A. Hammid, A. Raj, S. Stephen, T. Anjana, and V. Balasubramanian. 2018. On the characteristics and reactivity of soot particles from ethanol-gasoline and 2,5-dimethylfuran-gasoline blends. *Fuel* 222:42–55. doi: 10.1016/j.fuel.2018.02.147.

He, C. 2019. Radiative properties of atmospheric black carbon (soot) particles with complex structures. In *Springer series in light scattering, volume 4: Light scattering and radiative transfer*, ed. A. Kokhanovsky, 219–54. Basel: Springer Nature.

Heinrich, G., M. Klüppel, and T. A. Vilgis. 2002. Reinforcement of elastomers. *Curr. Opin. Solid State Mater. Sci.* 6 (3):195–203. doi: 10.1016/S1359-0286(02)00030-X.

Hiram, Y., and A. Nir. 1983. A simulation of surface tension driven coalescence. *J. Colloid Interface Sci.* 95 (2):462–70. doi: 10.1016/0021-9797(83)90206-0.

IPCC. 2014. *Climate Change 2014: Synthesis report. Contribution of working groups I, II and III to the fifth assessment report of the Intergovernmental Panel on Climate Change*. Technical report, ed. R. K. Pachauri and L. A. Meyer. Geneva: Core Writing Team.

Kelesidis, G. A., and S. E. Pratsinis. 2022. Santoro flame: The volume fraction of soot accounting for its morphology & composition. *Combust. Flame* 240:112025. doi: 10.1016/j.combustflame.2022.112025.

Kim, T., C. Ham, C. K. Rhee, S. H. Yoon, M. Tsuji, and I. Mochida. 2009. Effects of oxidation and heat treatment of acetylene blacks on their electrochemical double layer capacitances. *Carbon* 47 (1):226–33. doi: 10.1016/j.carbon.2008.10.010.

Kobata, A., K. Kusakabe, and S. Morooka. 1991. Growth and transformation of TiO_2 crystallites in aerosol reactor. *AlChE. J.* 37 (3):347–59. doi: 10.1002/aic.690370305.

Koch, W., and S. K. Friedlander. 1990. The effect of particle coalescence on the surface area of a coagulating aerosol. *J. Colloid Interface Sci.* 140 (2):419–27. doi: 10.1016/0021-9797(90)90362-R.

Kruis, F., K. A. Kusters, S. E. Pratsinis, and B. Scarlett. 1993. A simple model for the evolution of the characteristics of aggregate particles undergoing coagulation and sintering. *Aerosol Sci. Technol.* 19 (4):514–26. doi: 10.1080/02786829308959656.

Lamb, H. 1932. *Hydrodynamics*. 6th ed. Cambridge: Cambridge University.

Li, X., F. He, S. Hu, N. Sun, C. Huo, and R. Liu. 2023. The culprits of superoxide dismutase inactivation under size-dependent stress of ultrafine carbon black: Superoxide anion, genotoxicity and protein corona. *Sci. Total Environ.* 862:160770. doi: 10.1016/j.scitotenv.2022.160770.

Link, O., D. R. Snelling, K. A. Thomson, and G. J. Smallwood. 2011. Development of absolute intensity multi-angle light scattering for the determination of polydisperse soot aggregate properties. *Proc. Combust. Inst.* 33 (1):847–54. doi: 10.1016/j.proci.2010.06.073.

Liu, L., and M. I. Mishchenko. 2018. Scattering and radiative properties of morphologically complex carbonaceous aerosols: A systematic modeling study. *Remote Sens.* 10 (10):1634. doi: 10.3390/rs10101634.

Matsukawa, Y., K. Dewa, K. Era, T. Aoki, and H. Aoki. 2023. Experimental coalescence characteristic time of carbon nanoparticle produced from ethylene or benzene pyrolysis. *Chem. Eng. Res. Des.* 198:403–12. doi: 10.1016/j.cherd.2023.09.004.

Medalia, A. I., D. Rivin, and D. R. Sanders. 1983. A comparison of carbon black with soot. *Sci. Total Environ.* 31 (1):1–22. doi: 10.1016/0048-9697(83)90053-0.

Michelsen, H. A., M. B. Colket, P.-E. Bengtsson, A. D'Anna, P. Desgroux, B. S. Haynes, J. H. Miller, G. J. Nathan, H. Pitsch, and H. Wang. 2020. A review of terminology used to describe soot formation and evolution under combustion and pyrolytic conditions. *ACS Nano.* 14 (10):12470–90. doi: 10.1021/acsnano.0c06226.

Morgan, N. M., R. I. A. Patterson, and M. Kraft. 2008. Modes of neck growth in nanoparticle aggregates. *Combust. Flame* 152 (1–2):272–5. doi: 10.1016/j.combustflame.2007.08.007.

Nejar, N., M. Makkee, and M. Illangomez. 2007. Catalytic removal of NO_x and soot from diesel exhaust: Oxidation behaviour of carbon materials used as model soot. *Appl. Catal. B* 75 (1–2):11–6. doi: 10.1016/j.apcatb.2007.03.009.

Neoh, K. G. 1980. *Soot burnout in flames*. Ph.D. thesis, Massachusetts Institute of Technology.

Niranjan, R., and A. K. Thakur. 2017. The toxicological mechanisms of environmental soot (black carbon) and carbon black: Focus on oxidative stress and inflammatory pathways. *Front. Immunol.* 8:763. doi: 10.3389/fimmu.2017.00763.

Ogren, J. A. 1982. Deposition of particulate elemental carbon from the atmosphere. In *Particulate carbon*, ed. G. Wolff and R. Klimisch, 379–91. Boston, MA: Springer.

Ono, K., K. Dewa, Y. Matsukawa, Y. Saito, Y. Matsushita, H. Aoki, K. Era, T. Aoki, and T. Yamaguchi. 2017. Experimental evidence for the sintering of primary soot particles. *J. Aerosol Sci.* 105:1–9. doi: 10.1016/j.jaerosci.2016.11.013.

Park, S. H., and S. N. Rogak. 2004. A novel fixed-sectional model for the formation and growth of aerosol agglomerates. *Aerosol Sci.* 35 (11):1385–404. doi: 10.1016/j.jaerosci.2004.05.010.

Popovicheva, O. B., N. M. Persiantseva, B. V. Kuznetsov, T. A. Rakhmanova, N. K. Shonija, J. Suzanne, and D. Ferry. 2003. Microstructure and water adsorbability of aircraft combustor soots and kerosene flame soots: Toward an aircraft-generated soot laboratory surrogate. *J. Phys. Chem. A* 107 (47):10046–54. doi: 10.1021/jp034402f.

Quan, Y., Q. Liu, S. Zhang, and S. Zhang. 2018. Comparison of the morphology, chemical composition and microstructure of cryptocrystalline graphite and carbon black. *Appl. Surf. Sci.* 445:335–41. doi: 10.1016/j.apsusc.2018.03.182.

Rayleigh, L. 1879. On the capillary phenomena of jets. *Proc. R. Soc.* 29:71–97.

Rigopoulos, S. 2019. Modelling of soot aerosol dynamics in turbulent flow. *Flow. Turbulence Combust.* 103 (3):565–604. doi: 10.1007/s10494-019-00054-8.

Rigopoulos, S. 2024. *Population balance of particles in flows: From aerosols to crystallisation*. Cambridge, UK: Cambridge University Press.

Risby, T. H., and S. S. Sehnert. 1988. A model for the formation of airborne particulate matter based on the gas-phase adsorption on amorphous carbon blacks. *Environ. Health Perspect.* 77:131–40. doi: 10.2307/3430638.

Robertson, C. G., and N. J. Hardman. 2021. Nature of carbon black reinforcement of rubber: Perspective on the original polymer nanocomposite. *Polymers* 13 (4):538. doi: 10.3390/polym13040538.

Rogak, S. N. 1997. Modeling small cluster deposition on the primary particles of aerosol agglomerates. *Aerosol Sci. Technol.* 26 (2):127–40. doi: 10.1080/02786829708965419.

Ross, M. M., T. H. Risby, W. A. Steele, S. S. Lestz, and R. E. Yasbin. 1982. Physicochemical properties of diesel particulate matter. *Colloids Surf.* 5 (1):17–31. doi: 10.1016/0166-6622(82)80054-1.

Santamaria, A., N. Yang, E. Eddings, and F. Mondragon. 2010. Chemical and morphological characterization of soot and soot precursors generated in an inverse diffusion flame with aromatic and aliphatic fuels. *Combust. Flame* 157 (1):33–42. doi: 10.1016/j.combustflame.2009.09.016.

Santoro, R. J., H. G. Semerjian, and R. A. Dobbins. 1983. Soot particle measurements in diffusion flames. *Combust. Flame* 51:203–18. doi: 10.1016/0010-2180(83)90099-8.

Seto, T., M. Shimada, and K. Okuyama. 1995. Evaluation of sintering of nanometer-sized titania using aerosol method. *Aerosol Sci. Technol.* 23 (2):183–200. doi: 10.1080/02786829508965303.

Setyan, A., J. J. Sauvain, and M. J. Rossi. 2009. The use of heterogeneous chemistry for the characterization of functional groups at the gas/particle interface of soot and TiO_2 nanoparticles. *Phys. Chem. Chem. Phys.* 11 (29): 6205–17. doi: 10.1039/b902509j.

Shekar, S., A. J. Smith, W. J. Menz, M. Sander, and M. Kraft. 2012. A multidimensional population balance model to describe the aerosol synthesis of silica nanoparticles. *J. Aerosol Sci.* 44:83–98. doi: 10.1016/j.jaerosci.2011.09.004.

Spahr, M. E., and R. Rothon. 2015. Carbon black as a polymer filler. In *Encyclopedia of polymers and composites*, ed. S. Palsule, 1–24. Berlin, Heidelberg: Springer.

Studebaker, M. L., E. W. D. Huffman, A. C. Wolfe, and L. G. Nabors. 1956. Oxygen-containing groups on the surface of carbon black. *Ind. Eng. Chem.* 48 (1):162–6. doi: 10.1021/ie50553a044.

Sun, B., S. Rigopoulos, and A. Liu. 2021. Modelling of soot coalescence and aggregation with a two-population balance equation model and a conservative finite volume method. *Combust. Flame* 229:111382. doi: 10.1016/j.combustflame.2021.02.028.

Tang, R., J. Shang, X. Qiu, J. Gong, T. Xue, and T. Zhu. 2024. Origin, structural characteristics, and health effects of atmospheric soot particles: A review. *Curr. Pollut. Rep.* 10 (3):532–47. doi: 10.1007/s40726-024-00307-9.

Tsantilis, S., S. E. Pratsinis, and H. Briesen. 2001. Sintering time for silica particle growth. *Aerosol Sci. Technol.* 34 (3):237–46. doi: 10.1080/02786820150217812.

Tunnicliffe, L. B. 2015. *Particulate reinforcement of elastomers at small strains*. Ph.D. thesis, Queen Mary University of London.

Van Niekerk, J. E. 1994. *The numerical modelling of a carbon black oil furnace*. Ph.D. thesis, Imperial College London.

Veshkini, A., S. B. Dworkin, and M. J. Thomson. 2016. Understanding soot particle size evolution in laminar ethylene/air diffusion flames using novel soot coalescence models. *Combust. Theor. Model.* 20 (4):707–34. doi: 10.1080/13647830.2016.1169319.

Vu, T. V., S. Zauli-Sajani, V. Poluzzi, and R. M. Harrison. 2018. Factors controlling the lung dose of road traffic-generated sub-micrometre aerosols from outdoor to indoor environments. *Air Qual. Atmos. Health* 11 (6): 615–25. doi: 10.1007/s11869-018-0568-2.

Wang, L., C. Song, J. Song, G. Lv, H. Pang, and W. Zhang. 2013. Aliphatic C–H and oxygenated surface functional groups of diesel in-cylinder soot: Characterizations and impact on soot oxidation behavior. *Proc. Combust. Inst.* 34 (2):3099–106. doi: 10.1016/j.proci.2012.07.052.

Wang, M. J., C. A. Gray, S. A. Reznek, K. Mahmud, and Y. Kutsovsky. 2003. Carbon black. *Kirk-Othmer Encycl. Chem. Technol.* 11:761–803. doi: 10.1002/0471238961.0301180204011414.a01.pub2.

Wolff, G. T. 1985. Characteristics and consequences of soot in the atmosphere. *Environ. Int.* 11 (2–4):259–69. doi: 10.1016/0160-4120(85)90018-2.

Wu, M. K., C. K. Steiner, R. S. Windeler, C. K. Steiner, T. Börs, and S. K. Friedlander. 1993. Controlled synthesis of nanosized particles by aerosol processes. *Aerosol Sci. Technol.* 19 (4):527–48. doi: 10.1080/02786829308959657.

Xiong, Y., M. Kamal Akhtar, and S. E. Pratsinis. 1993. Formation of agglomerate particles by coagulation and sintering—Part II. The evolution of the morphology of aerosol-made titania, silica and silica-doped titania powders. *J. Aerosol Sci.* 24 (3):301–13. doi: 10.1016/0021-8502(93)90004-S.

Zhao, B., Z. Yang, Z. Li, M. V. Johnston, and H. Wang. 2005. Particle size distribution function of incipient soot in laminar premixed ethylene flames: Effect of flame temperature. *Proc. Combust. Inst.* 30 (1):1441–8. doi: 10.1016/j.proci.2004.08.104.

Appendix A

In this appendix, we show that the assumption of 10/90 split between nucleation and growth does not have a significant effect on the initial primary particle size. Nascent soot nuclei can be viewed as spheres of 1 nm in diameter. If growth is responsible for 90% of the conversion from feed to product, this would cause the volume of these nuclei to increase by a factor of 10. Therefore:

- Let $d_{nuc} = 1\,\text{nm}$ and $v_{nuc} = \frac{\pi}{6} d_{nuc}^3$.
- Thus, growth causes a 10-fold increase in volume: $v_0 = 10\ v_{nuc}$.
- The scaling in diameter can be recovered as $d_0 = \sqrt[3]{10}\ \text{d}_{nuc}$.
- More generally for a volume increase factor due to growth, A, we have $d_0 = \sqrt[3]{A}\ \text{d}_{nuc}$.

Table A1 shows the d_0 computed for different values of nucleation/growth split. It can be seen that the d_0 is not very sensitive to this factor.

Table A1. Initial primary particle diameters as a function of nucleation/growth split.

Growth (%)	Nucleation (%)	Volume increase factor, A	Diameter increase factor	d_0 (nm)	$T_a(K)$	m
90	10	10	$\sqrt[3]{10} = 2.15$	2.15	15,617	$m = 1$
95	5	20	$\sqrt[3]{20} = 2.71$	2.71	15,296	$m = 1$
99	1	100	$\sqrt[3]{100} = 4.64$	4.64	14,165	$m = 1$